Tellus (2006), 58B, 163–176
Printed in Singapore. All rights reserved

TELLUS

Evaluation of 2001 springtime CO transport over West Africa using MOPITT CO measurements assimilated in a global chemistry transport model

By STÉPHANIE PRADIER[1]*, JEAN-LUC ATTIÉ[2], MICHEL CHONG[2], JUAN ESCOBAR[2], VINCENT-HENRI PEUCH[1], JEAN-FRANÇOIS LAMARQUE[3], BORIS KHATTATOV[3] and DAVID EDWARDS[3], [1]*CNRM, Météo-France, Av. Coriolis, Toulouse, France;* [2]*Laboratoire d'Aérologie, UMR 5560 (CNRS/UPS), 14 Av. Edouard Belin, Toulouse, France;* [3]*NCAR, ACD, 1850 Table Mesa Drive, Boulder CO, 80307, USA*

(Manuscript received 3 February 2005; in final form 6 February 2006)

ABSTRACT

The global chemistry and transport model MOCAGE (Modèle de Chimie Atmosphérique à Grande Echelle) is used to investigate the contribution of transport to the carbon monoxide (CO) distribution over West Africa during spring 2001. It is constrained with the CO profiles provided by the Measurements Of Pollution In The Troposphere (MOPITT) instrument through a sequential assimilation technique based on a suboptimal Kalman filter. The improvement of tropospheric CO distribution from MOCAGE is evaluated by comparing the model results (with and without assimilation) with the MOPITT CO concentrations observed during the analysed period (between 2001 March 15 to 2001 April 30), and also with independent *in situ* CMDL and TRACE-P observations. The initial overestimation in high CO emissions areas (Africa, SE Asia and NW coast of South America) is considerably reduced by using the MOPITT CO assimilation. We analysed the assimilated CO for a period of three successive 15 d periods in terms of average fields over West Africa and contributions to the CO budget of transport and chemical sources. It is found that the horizontal and vertical CO distributions are strongly dependent on the characteristics of the large-scale flows during spring, marked by the onset of the low-level southerly monsoon flow and the gradual increase of the well-known African and tropical easterly jets at middle and upper levels, respectively. Total transport by the mean flow (horizontal plus vertical advection) is important in the CO budget since it mostly compensates the local sink or source generated by chemical reactions and small-scale processes. The major source of CO is concentrated in the lower troposphere (1000–800 hPa) mainly due to convergent low-level flow advecting CO from surrounding regions and surface emissions (biomass burning). Vertical transport removes 70% of this low-level CO and redistributes it in the middle troposphere (800–400 hPa) where chemical reactions and horizontal exports contribute to the loss of CO. A lesser proportion is transported upwards into upper troposphere, and then horizontally, out of the considered domain.

1. Introduction

Knowledge of the CO distribution is essential to determine the chemical activity in the troposphere through its dominant role in the tropospheric OH radical depletion (Thompson, 1992), and also to identify the main sources of pollution such as biomass burning. Increased CO may also indirectly affect the radiative forcing of the atmosphere and hence intensify the global warming by increasing the concentration of greenhouse gases such as ozone (O_3) and other oxidants (Daniel and Solomon, 1998). It is widely recognized that the tropospheric distribution of CO and other chemical species is strongly modulated by atmospheric processes. In particular, vertical and long-range horizontal transports are major contributions to the export of polluted air from one region to another or between continents (Bey et al., 2001a). Due to its relatively long life time [2 months on global average (Cicerone, 1988)] and the large variability of its source and distribution, the CO can be used as a tracer to diagnose the tropospheric circulation and main pollution outflow regions. At present, the predominant pollution sources are identified over the globe, and the main pathways of intercontinental air transport are known (Stohl et al., 2002; Duncan and Bey, 2004; Liang et al., 2004). However, a better characterization of all transport processes is still needed since a wide range of spatial scales, physical and chemical mechanisms, is involved (Mari et al., 2003). An increasing interest is taken in the most polluted

*Corresponding author.
e-mail: stephanie.pradier@cnrm.meteo.fr
DOI: 10.1111/j.1600-0889.2006.00185.x

continents, such as North America or Asia, as targets of aircraft campaigns [NARE (Fehsenfeld et al., 1996), PEM-West B (Hoell et al., 1997), TRACE-P (Jacob et al., 2003)]. The present study focuses on African continent, and more specifically on West Africa, which is known to generate huge amounts of pollutants from both its megalopolis concentrated around Gulf of Guinea and biomass burning during winter time. Considering CO anthropogenic emissions from domestic and industrial activities, Stohl et al. (2002) characterized the timescales and the pathways of intercontinental transport all year long; this study shows that African CO tracer experiences strong up lifting. That plume stays mostly confined to the tropics because of subtropical transport barriers, tracers crossing Atlantic Ocean in 25–30 d. But, depending on the season, emissions from northern and southern Africa can be advected towards the midlatitude stormtracks, and so reach European or Australian continents. Analysing the CO emitted from the northern Africa biomass burnings in the early part of the year, Edwards et al. (2003) also underlined the vertical transport in the free troposphere, and its export westwards out into the Atlantic, and southwestwards to the Gulf of Guinea or southern central Africa (fires in western and eastern Africa, respectively). Whereas Africa outflow of CO is confirmed, it is necessary to quantify its intensity in order to better characterize its impact on the tropospheric chemistry. This is one of the goals of AMMA (African Monsoon Multidisciplinary Analysis, http://amma.mediasfrance.org/international/index), an international project of which the Special Observing Periods (SOP) will be held in 2006. AMMA implements both numerical and satellite tools upstream, during and downstream the SOPs. The study proposed here constitutes a preliminary work to the AMMA campaign.

Global Chemistry and Transport Models (CTM) including assimilation of chemical species measurements (e.g. Allen et al., 1996; Lamarque et al., 1999; Khattatov et al., 2000; Cathala et al., 2003) are used for a better understanding of global atmospheric chemistry. The chemical assimilation part allows constraining the distributions of observed species (and also possibly of non-observed but chemically related species) while meteorological analyses give realistic forcing. The assimilation provides global 4-D fields by combining model fields and data, which are well suited for budget analyses. In this study, Measurements Of Pollution In The Troposphere (MOPITT) CO data (Drummond, 1992; Edwards et al., 2003) are used to constrain the Modèle de Chimie Atmosphérique à Grande Echelle (MOCAGE) CTM (Peuch et al., 1999), using the assimilation procedure described in Khattatov et al. (2000) and based on the Kalman-Bucy filter. Transport processes in MOCAGE are discussed and evaluated in Josse et al. (2004). The purpose of this paper is to evaluate the CO transport over West Africa by assimilating MOPITT CO in the MOCAGE model, after validating the assimilation procedure with independent *in situ* data. Sections 2 and 3 give an overview of the MOPITT CO data and the MOCAGE model, respectively. The assimilation technique is described in Section 4 and its validation is performed in Section 5. In Section 6, we analyse the average springtime CO distribution along with the airflow structure; last, the CO transport and budget over West Africa are discussed in Section 7.

2. MOPITT CO observations

MOPITT measurements are performed in eight nadir-viewing spectral channels using the gas correlation technique. Detailed description of the instrument can be found in Drummond (1992) and Drummond and Mand (1996). The MOPITT CO data consist of total column and vertical profiles of volume mixing ratio that are retrieved at seven pressure levels (surface, 850, 700, 500, 350, 250 and 150 hPa), with a horizontal resolution of 22 $\times$ 22 km^2. Global coverage is accomplished in 3–4 d and data are available from 2000 March to present. The version 3 level 2 CO profiles (available on the NASA Langley DAAC) are used in the present study and are by-products of an operational retrieval algorithm (Deeter et al., 2003), the so-called 'maximum *a posteriori*' (MAP) solution based on an optimal estimation method (Pan et al., 1998; Rodgers, 2000). The retrieval of CO profiles from MOPITT calibrated radiances is based on three of the planned signal channels.

The retrieved profile $\mathbf{x}_r$ can be expressed as a weighted mean of the true unknown profile $\mathbf{x}$ and an *a priori* profile $\mathbf{x}_a$ through the matrix relationship

$$\mathbf{x}_r \approx \mathbf{x}_a + \mathrm{A}(\mathbf{x} - \mathbf{x}_a) = \mathbf{A}\mathbf{x} + (\mathbf{I} - \mathbf{A})\mathbf{x}_a, \quad (1)$$

where $\mathbf{I}$ is the identity matrix and $\mathbf{A}$ is the matrix in which each row defines the averaging kernel (Rodgers, 2000) for one particular level of the retrieved profile. The *a priori* term describes the expected statistical behaviour of the CO profile, deduced from an extended set of *in situ* data (Deeter et al., 2003). The *a priori* contribution $(\mathbf{I} - \mathbf{A})\mathbf{x}_a$ reflects the smoothing error (Rodgers, 1990). The lower this contribution, the closer the retrieved value is to the true state. In this study, we arbitrarily discarded CO MOPITT profiles with more than 40% *a priori* contribution at 500 hPa. This level is considered as the most significant in terms of MOPITT CO measurement. The MOPITT validation, based on a large set of CO profiles collected during aircraft flights, indicates more important biases in the lower troposphere (4–5 ppbv) (Emmons et al., 2004). Values in percentage range from $8.1 \pm 21.5\%$ at ground level to $3.8 \pm 10.1\%$ at 500 hPa, and to $-0.2 \pm 15.8\%$ at 150 hPa. The 500 hPa level is characterized by the lowest bias standard deviation. At this level, MOPITT averaging kernels show highest sensitivity in the middle and upper troposphere (Deeter et al., 2004). However, they exhibit significant variability mostly related to the variability of the atmospheric temperature profile, surface pressure, and actual CO profile. In particular, diurnal variations of surface temperature have considerable effects yielding quite different daytime and nighttime kernels. Mean averaging kernels (Deeter et al., 2003) reveal this variability and their geographical location and seasonal

dependence. It can be shown (Rodgers, 2000) that the averaging kernel matrix **A** is related to the *a priori* error covariance matrix $\mathbf{C}_a$ and retrieved error covariance matrix $\mathbf{C}_x$ through

$$\mathrm{A} = \mathrm{I} - \mathbf{C}_x \mathbf{C}_a^{-1}. \quad (2)$$

Knowledge of the measurements errors $\mathbf{C}_x$ is essential for the sequential assimilation technique described in the next section, and they are included in the MOPITT datasets.

3. Model description

MOCAGE is a global three-dimensional chemistry and transport model developed at the Centre National de Recherches Météorologiques of Météo-France, dedicated to the numerical simulation of the interactions between dynamical, physical and chemical processes in the troposphere and lower stratosphere (Peuch et al., 1999). It is a semi-lagrangian gridpoint model, which can run with up to four levels of nested domains (two-way nesting), with resolution down to 10 km over areas of special interest. In this study, only the global domain of MOCAGE at a resolution of 2° is considered. The vertical grid is composed of 47 hybrid (σ, P) levels from the surface to 5 hPa, with typical resolutions of 40–400 m in the boundary layer (seven levels) and about 800 m near the tropopause and in the lower stratosphere. ARPEGE (Courtier et al., 1991) meteorological analyses are used to initialize and constrain the model every 6 hr. Concerning the wind components, only zonal and meridional values are taken from ARPEGE. Vertical velocity is calculated from these horizontal components by imposing mass conservation for each vertical atmospheric column. Convective processes are simulated with the scheme of Bechtold et al. (2001), and turbulent diffusion is calculated with scheme by Louis (1979). Overall model performances in terms of transport at resolved and subgrid scales are described by Josse et al. (2004). MOCAGE takes into account the comprehensive chemical scheme RACMOBUS which is the merging of two detailed stratospheric and tropospheric chemical schemes, REPROBUS (Lefèvre et al., 1994) and RACM (Stockwell et al., 1997). RACMOBUS includes 119 individual species or groups of species, among which 89 are prognostic variables, and it considers 372 chemical reactions. MOCAGE also uses parametrization schemes relative to emission and dry deposition (Michou and Peuch, 2002; Nho-Kim et al., 2004; Michou et al., 2005), and scavenging. MOCAGE is now used daily for chemical weather forecasts (Dufour et al., 2005; see also http://www.prevair.org).

In the present study, the time step for the evolution of chemical constituents due to physical and chemical processes is 15 min while dynamical changes are calculated every hour. An operator splitting approach is used and the different parametrizations are called in alternating order at each third step of 15 min. The model is run with (referred as MOCAGE-ASSIM) and without (referred as MOCAGE-NOASSIM) assimilation of MOPITT CO from 2001 March 1 to 2001 May 6. The initial field of CO on 2001 March 1 is provided by the National Center for Atmospheric Research climatology that is used in the global 3-D chemical transport model MOZART (Model of Ozone and Related Chemical Tracers). Monthly emissions of CO are those supplied by IIASA, and spatially distributed using the EDGAR3.2 database (Olivier et al., 1996), as described in Dentener et al. (2005). It yields a CO total emission of 1046 Tg CO yr^{-1}, with 575 Tg CO yr^{-1} from biomass burning. These values are in agreement with the range of CO emissions used in some other global models. For example, Bey et al. (2001b), Horowitz et al. (2003) and Granier et al. (2000) use a global source of 1043, 1195.05 and 1337 Tg CO yr^{-1}, respectively, with biomass burning contribution of 550, 486.63 and 675 Tg CO yr^{-1}. Figure 1 shows the fire positions seen by TRMM/VIRS (Giglio et al., 2003) over Africa for 2001 March and April, and the CO emissions used in MOCAGE. Most of fires are located between 15°N and 10°S for the 2 months. But, during April, the number of fire counts decreases in the Northern hemisphere, and increases in the Southern one. The timing and localization is consistent with CO emissions inventory used for our simulations. It should be noted that Figs. 1(c) and (d) indicate also emissions due to industrial activity, in particular around the Gulf of Guinea. These emissions are similar for the March and April months.

4. Assimilation procedure

The data assimilation technique described in Lamarque et al. (1999) and Khattatov et al. (2000) is applied every hour, with an assimilation window of 1 hr. It consists of a suboptimal Kalman filter that uses the model forecast at the beginning of this window as the background field, with an explicit calculation of the forecast error variance. The basic equation follows the optimal interpolation equation of Lorenc (1986)

$$\mathbf{w}_t^a = \mathbf{w}_t^f + \mathrm{K}_t\left(\mathbf{w}_t^o - \mathbf{H}_t \mathbf{w}_t^f\right), \quad (3)$$

where $\mathbf{w}_t{}^a$ is the analysed field, $\mathbf{w}_t{}^f$ is the model background field and $\mathbf{w}_t{}^o$ is the observational dataset in the assimilation window centred around the current model time t. To simplify the notation, subscript t will be ignored hereafter. **H** is the observational operator that enables the calculation of model CO profiles to be compared to the MOPITT retrieved profiles through eq. (1), where **x** represents the model background values at the location of the observed profiles. Therefore, it combines a horizontal interpolation to the geographical location of the observation, a vertical interpolation to the retrieval pressure levels, and an application of the corresponding averaging kernel. **K** is the Kalman gain matrix defined as

$$\mathrm{K} = \mathbf{B}\mathbf{H}^T(\mathbf{H}\mathbf{B}\mathbf{H}^T + \mathbf{O} + \mathbf{R})^{-1}, \quad (4)$$

where **B** is the forecast error covariance matrix, **O** contains the error covariance matrices $\mathbf{C}_x$ of the observations, and **R** is the representativeness error covariance matrix associated with errors

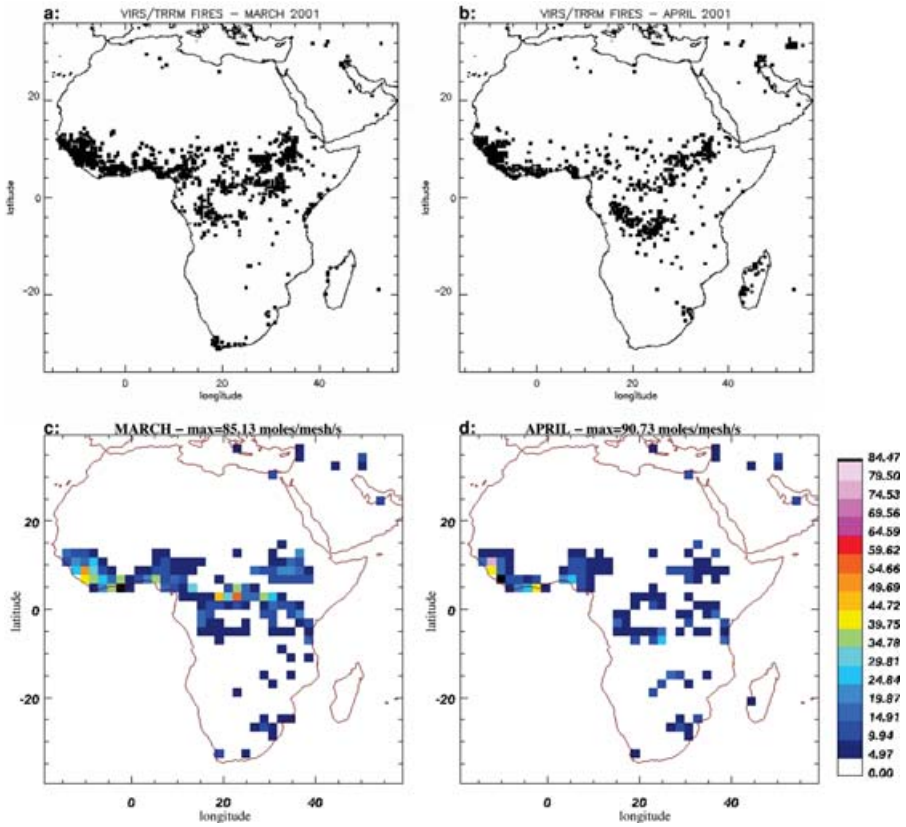

Fig. 1. Fires map (0.5° resolution) over Africa provided by VIRS/TRMM instrument for 2001, March (a) and April (b), and CO monthly emissions inventory used in MOCAGE for March (c) and April (d) (moles mesh^{-1} s^{-1})

of interpolation and discretization. In the following, **R** is assumed to be negligible.

The diagonal elements of **B** or forecast error variances are explicitly calculated during the assimilation run, with initial errors taken as 30% of the model CO field. Off-diagonal elements are parametrized by separate Gaussian functions depending on the horizontal and vertical distance between the considered points, with specific influence radii of 200 and 0.7 km defining the horizontal and vertical correlation lengths, respectively. At each assimilation cycle, the forecast error covariance is updated by the analysis error covariance defined as (Lorenc, 1986)

$$\mathbf{B}^a = (\mathbf{I} - \mathbf{KH})\mathbf{B},$$

and the evolution of the modified forecast variance is calculated by integrating the chemical model forward with the updated variance as initial conditions. However, as discussed in Khattatov et al. (2000), an additional model error growth is required to take into account the imperfections of the model that would lead to diverging solutions, and it is assumed to be proportional to the modelled field and the 1 hr integration period. The proportionality coefficient is set to 0.005 per hour.

The above various parameters (initial errors, correlation lengths, error growth, representativeness error) have been adjusted for satisfying the following chi-square diagnosis (Ménard et al., 2000)

$$\chi^2 = \left(\mathbf{w}^o - \mathbf{H}_t\mathbf{w}^f\right)^{\mathrm{T}}(\mathbf{HBH}^T + \mathbf{O} + \mathbf{R})^{-1}(\mathbf{w}^o - \mathbf{Hw}^f) = N,$$

where N is the total number of independent measurements involved in the determination of all assimilated profiles (for a particular profile, the trace of the averaging kernel matrix gives the number of independent elements). Throughout the 2 month assimilation period, the associated χ^2/N ratios oscillate around 1, suggesting that the selected parameters are well suited.

5. Validation

An in short evaluation test consists of a systematic comparison of the model results from MOCAGE-ASSIM and MOCAGE-NOASSIM runs with the observed MOPITT CO measurements that were used in the assimilation procedure. Model outputs were saved every 6 hr. So before applying the appropriate averaging kernels to the model values that enable a point-to-point comparison, the model fields are interpolated according to the space–time coordinates of the observations. The linearity assumption is correct 5 d after the beginning of the simulation as revealed in particular by the time evolution of the χ^2/N ratios (not shown).

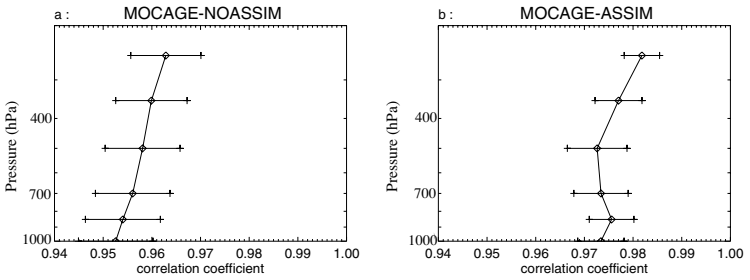

Fig. 2. Pearson correlation coefficient of MOPITT and MOCAGE, without (a) and with (b) assimilation. Error bars are indicated.

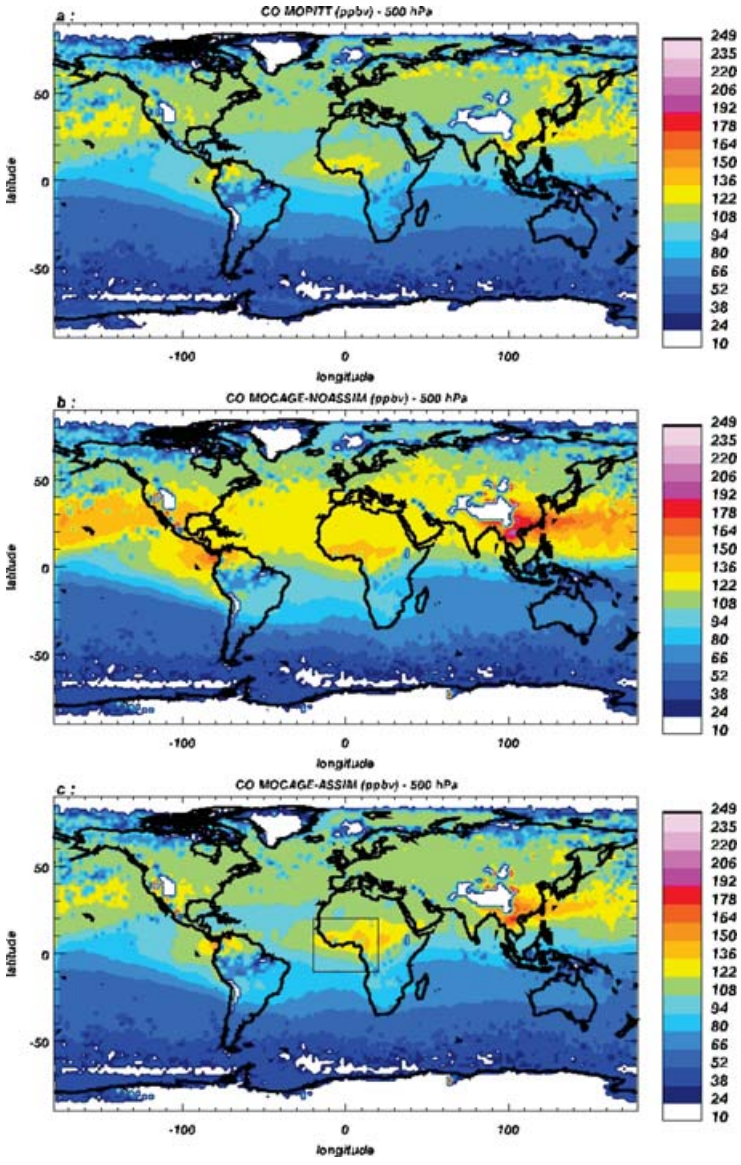

Fig. 3. Mean global CO distributions (ppbv) at 500 hPa from (a) MOPITT measurements, (b) MOCAGE without assimilation and (c) MOCAGE with assimilation. The square delimits the considered domain.

The analysed period begins on 2001 March 15 and ends on April 30. Figure 2 shows the mean, minimum and maximum for three 15-d-averaged linear Pearson coefficients of MOPITT and MOCAGE CO global distributions calculated at MOPITT levels. This figure clearly shows the stronger correlation between observations and simulation when the assimilation is performed. The correlation coefficients are around 0.955 with a mean error of 0.01 for MOCAGE-NOASSIM, while they increase to about 0.975 for MOCAGE-ASSIM, with a mean error decreasing to 0.005.

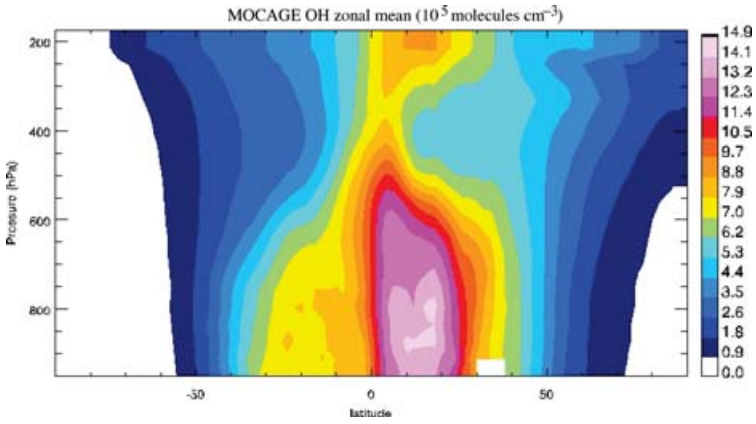

Fig. 4. MOCAGE OH mean zonal distribution (10^5 molecules cm^{-3}) averaged on 2001 April.

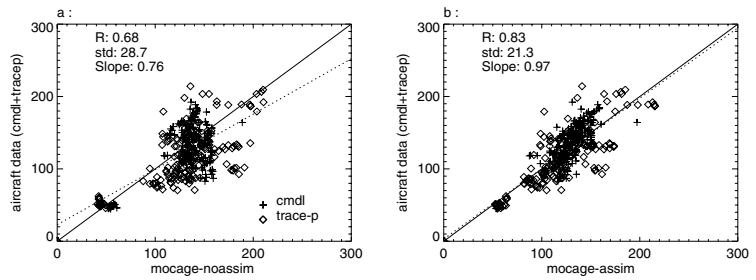

Fig. 5. Point-by-point global comparison of aircraft data (plus and diamond for CMDL and TRACE-P data, respectively) and corresponding MOCAGE simulations, (a) without MOPITT CO assimilation and (b) with assimilation. Also shown is the linear regression (dotted line) and the 1:1 relationship (continuous line). The slope of the linear regression and the corresponding correlation coefficient (R) and standard deviation (STD) are indicated.

Figure 3 compares the average distributions of CO at 500 hPa during the period of interest. Globally, MOPITT, MOCAGE-NOASSIM and MOCAGE-ASSIM show similar distributions with high CO concentrations in the northern hemisphere and tropical regions. The importance of MOPITT data to constrain the model simulations is highlighted by the close correlation between observed (Fig. 3a) and assimilated (Fig. 3c) CO fields, which appear quite comparable in magnitude and spatial extension. Significant differences can be found when the model runs are performed without assimilation (Fig. 3b). In most respects, MOCAGE-NOASSIM overestimates the CO mixing ratios, particularly over high CO emissions regions (equatorial Africa, SE Asia and NW coast of S. America). Several reasons could lead to this, for example uncertainties in the emission inventory, transport or chemical processes. Josse et al. (2004) have already described the validation of the model transport processes at the resolved and subgrid scales, using radon global simulation as in Jacob and Prather (1990) and Jacob et al. (1997). MOCAGE performs well at both scales. Concerning CO chemistry, and the related distribution of OH, the simulation performed by MOCAGE-NOASSIM presents expected features (Fig. 4): highest OH values are found in the tropical mid-troposphere reflecting the abundance of UV radiation and water vapour. However, OH maxima are lower by approximately 20% compared to recent estimates by Spivakovsky et al. (2000). This partly explains high CO concentrations. The assimilation of MOPITT CO tends to improve both CO and OH distributions (not shown) by increasing OH by about 5%. MOCAGE was previously used in several studies, in particular Dufour et al.'s (2005) work, in which heavy pollution episodes were simulated and compared to a 4-D air quality observations database (ozone, nitrogen oxides, radicals, volatile organic compounds measurements).

In order to assess the validity of CO assimilated fields, we made a comparison between MOCAGE-ASSIM CO and independent aircraft data measured in various experiments. We use 20 CO profiles from the Climate Monitoring and Diagnostics Laboratory (CMDL) (Novelli et al., 1992, 1998) and Transport and Chemical Characterization and Evolution over the Pacific experiment (TRACE-P) (Jacob et al., 2003) within the period. Figure 5 shows the comparison between these profiles and MOCAGE results with and without assimilation. The CMDL measurements were recorded over the North American continent and Western Pacific Ocean, TRACE-P data concern Eastern Asia coast. The improvement of the model representation of the CO mixing ratios using assimilation of MOPITT data is quite reasonable for these regions: the model-observation correlation increases (from 0.68 to 0.83) and the standard deviation decreases (from 28.7 to 21.3 ppbv). This correction is much more effective when considering the linear regression curve which has a slope of 0.97. In the case of MOCAGE-NOASSIM, the slope is 0.76. In the same way, Emmons et al. (2004) used CMDL and TRACE-P data among others sources, and compared them to MOPITT CO measurements for two periods: 2000 March–2001 May, and 2001 August–2002 December. For the first phase, which includes our study period, the mean Pearson correlation coefficient is about 0.87, a value comparable to our correlation coefficient of 0.83, with these

following differences (1) we worked on 2 months instead of the full year, (2) we considered a reduced set of data and (3) the horizontal and vertical resolutions in the model are quite different from the aircraft observations. Considering the horizontal resolution, the size mesh of MOCAGE is 2° and 22 km for MOPITT (pixel size). Nevertheless, this suggests that MOCAGE-ASSIM simulations provide 4-D CO fields of very good quality, which added to realistic meteorological forcing (ARPEGE analyses) give a more powerful tool to analyse budgets of CO than the model results without assimilation.

6. Dynamics and CO distribution

In this section the CO distribution over West Africa, along with the major meteorological features, is analysed during 2001 March and April. We consider the area bounded by 10°S, 20°N, 20°W and 20°E, which is a region of observed high CO concentration as shown in Fig. 3c, and corresponding to the large-scale AMMA observing region. March and April are particularly interesting months for two reasons. First, they correspond to the end of the northern hemisphere winter during which biomass burning takes place in Savannah regions and tropical rain forests of northern Africa, so large amounts of CO produced by incomplete combustion are emitted over burnt areas (Gregory et al., 1996; Cautenet et al., 1999; Nielsen, 1999). Second, they represent the onset period of southwesterly flux towards the south-facing coast of West Africa, originating from the southern hemisphere easterly trade winds as they cross the equator. This monsoon flux migrates further to the North during the boreal summer, and the position of the Intertropical Convergence Zone (ITCZ) between this flux and the northern hemisphere easterly winds, strongly modulates the tropospheric circulation and meteorological events in West Africa (see Leroux, 2001). The ITCZ is a region of rising air and corresponds to the ascending branch of the Hadley circulation. Towards the North, the tropospheric circulation is marked by dry easterly winds, the so-called Harmattan flow, that could extent from the surface to 600 hPa above which extratropical westerlies are blowing. The region of strongest wind intensity is located near the tropopause (100–200 hPa) and is referred hereafter as to the subtropical westerly jet (SWJ). Towards the South and above the monsoon flow of about 1000 m depth, easterly winds are dominant with two modes of strongest winds: the African easterly jet (AEJ) in the mid-layers (400–700 hPa) and the tropical easterly jet (TEJ) in the upper layers (100–200 hPa). During the northward migration of the ITCZ, the confrontation of the monsoon flux from the Gulf of Guinea and the Harmattan flow can be to the source of convective activity that is often organized in squall line moving from east to west, due to perturbations associated with large-scale easterly waves.

Figure 6 shows CO calculated by MOCAGE-ASSIM and wind fields at 850, 500 and 250 hPa. These represent an average over a 15 d period, namely from 1 to 15 April. The overall

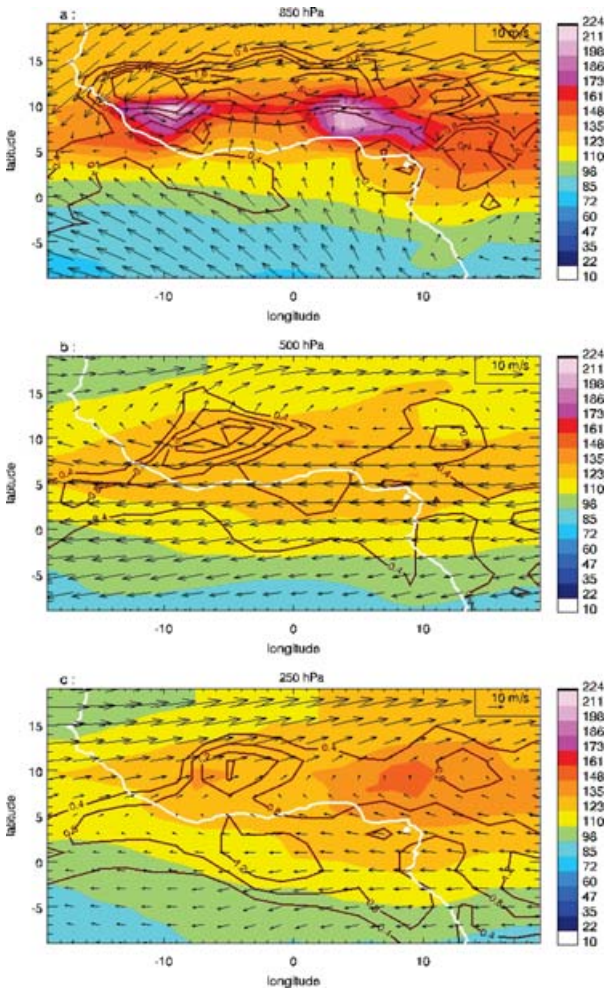

Fig. 6. Mean CO (colours, ppbv) and wind fields for the two first weeks of April (AP1) simulated by MOCAGE with assimilation of MOPITT CO, at 850 (a), 500 (b) and 250 hPa (c). Vertical velocity component is represented by isolines from 0.4 cm s^{-1}, and every 0.4 cm s^{-1}. African coast is also indicated (white isoline).

dynamical characteristics discussed above are well represented. The extensive west-east oriented area of high CO concentration (>150 ppbv) at 850 hPa (Fig. 6a) reveals the approximate position of biomass burning emissions. At middle and upper levels (Figs. 6b and c) the CO concentration is smaller, but it expands over a larger area. Near the surface, the northern border of high CO values domain is correlated with maximized positive vertical velocities (Fig. 6a), in the confluence zone of the Harmattan and monsoon flows. A major feature of CO field versus altitude is to present a minimum at mid-levels, which is well connected to the AEJ between 0° and 5°N (Fig. 6b). One can also note the westerly winds at 500 hPa beyond 15°N, with maximum intensity of 13 m s^{-1}. At higher levels (Fig. 6c), there is a clear signature of the SWJ (maximum intensity of 30m s^{-1}) beyond 10°N and the TEJ between 0 and 5°S, with the strongest CO between both jets.

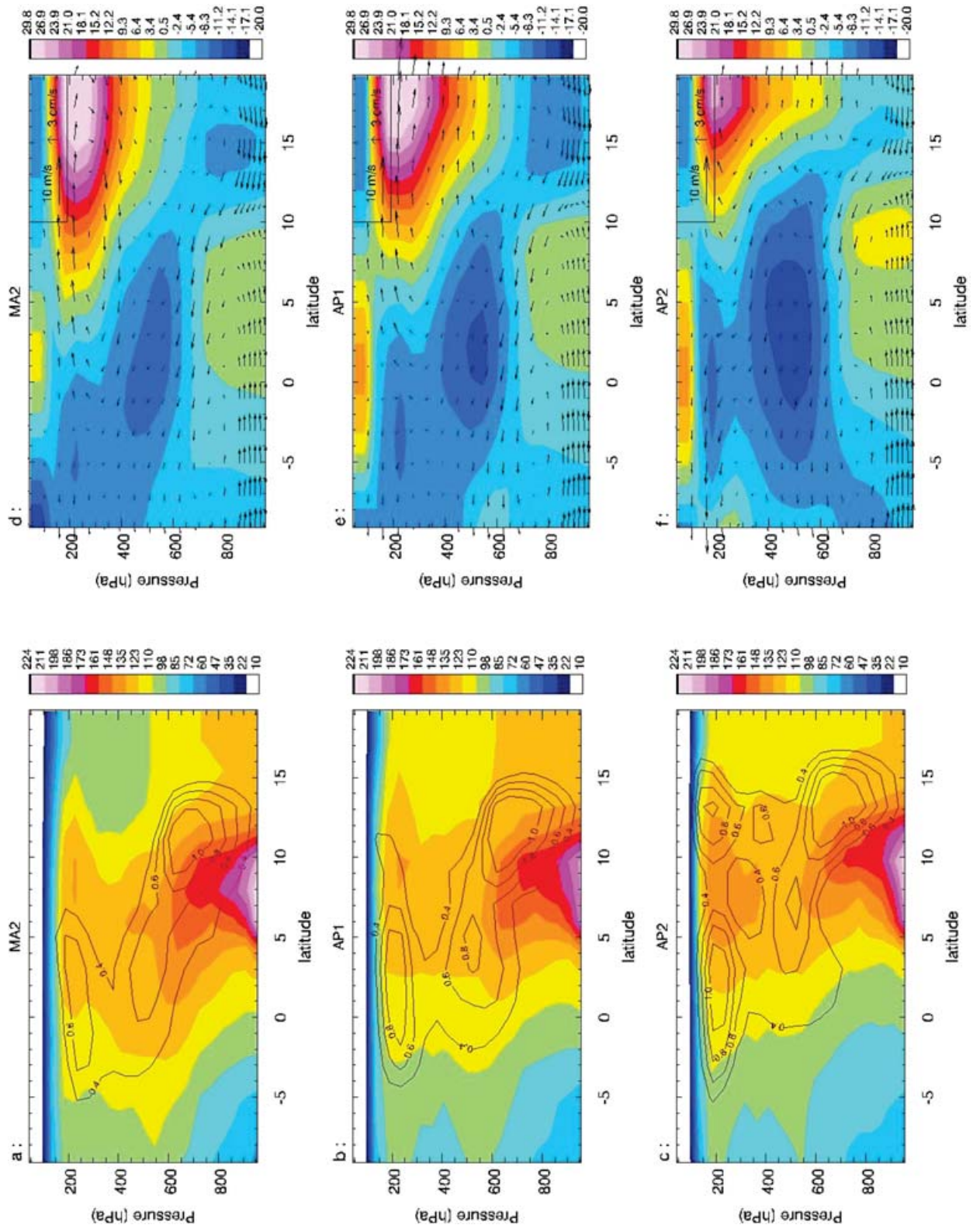

Fig. 7. Vertical mean CO and wind fields averaged over west-east extent of the Fig. 6 domain, and simulated by MOCAGE with assimilation for the three periods: (a, d) MA2, (b, e) AP1, and (c, f) AP2. Left column shows CO fields (ppbv) with vertical velocity (isolines, from 0.4 cm s^{-1} and every 0.2 cm s^{-1}). Right column shows longitudinal wind component intensity (m s^{-1}) and latitudinal airflow (arrows).

Figure 7 shows the evolution and organization of mean CO and wind fields along a meridional cross-section. The fields are averaged both in time, over three 15 d periods (15–31 March, 1–15 April and 16–30 April, hereafter referred to as MA2, AP1 and AP2, respectively), and space over the longitudinal width of the domain shown in Fig. 3c. The CO distribution indicates strong concentration near the surface, between 5° and 15°N, and more moderate values at higher levels, extending southwards and strengthening with time (Figs. 7a–c). Inspection of Figs. 7d–f reveals the gradual northward migration of the monsoon flow and also the other flow components in West Africa, that is, the northern hemisphere trade winds, AEJ, TEJ and SWJ. These jets influence the distribution of CO, particularly above 500 hPa. This level corresponds to the altitude at which the Harmattan flow transports the air mass enriched with CO. Above it, a part of this CO is swept away westwards by the AEJ, and another part is transferred upwards into the secondary circulations of the SWJ and TEJ. This is consistent with the two areas of positive vertical motion: the first from 850 to 500 hPa, and the second above, from 500 to 150 hPa (Figs. 7a–c). It should be noted that the upper core of ascending motion increases with time, in particular between MA2 and AP1/AP2. In fact, the northward displacement of the global circulation is faster in altitude: the secondary circulation of the SWJ and TEJ takes over efficiently from the upward motion generated at the surface, particularly during AP1. So air rich in CO penetrates more quickly through 250 hPa level into a region of weak horizontal winds (Fig. 6c). This extends, in a temporal way, the discussion of Edwards et al. (2003) about the CO transport near the ITCZ. Using forward trajectory, these authors evidence the influence of the horizontal advection, westwards and southwestwards for emissions from western and eastern Africa, respectively, as indicated in introduction. So, large-scale vertical motions generated in the upper troposphere by the ascending branch of the Hadley circulation, SWJ and AEJ have a clear impact on CO distribution during March and April.

7. CO transports over West Africa

The CO budget over a region is computed according to the calculation of Yanai et al. (1973) for the apparent heat source of a large-scale convective system, by considering the horizontal average of the conservation equation. Following Brasseur et al. (1999), in chemical models, the continuity equation can be explained as

$$\frac{\partial \rho r}{\partial t} = \underbrace{-\frac{\partial \rho u r}{\partial x} - \frac{\partial \rho v r}{\partial y} - \frac{\partial \rho w r}{\partial z}}_{T} + S + \Sigma, \tag{5}$$

where ρ is the air density (kg m^{-3}), r is the CO concentration (moles kg^{-1}), S and Σ are local sources/sinks (expressed in moles m^{-3} s^{-1}). S is due to chemical reactions. Σ represents the subgrid-scale processes that are parametrized in MOCAGE: turbulent diffusion, deep convection, wet scavenging, etc. as well as ground emissions and dry deposition. u, v and w are the zonal, meridional, and vertical wind components (m s^{-1}), respectively. $\partial/\partial t$ is the Eulerian derivative. T stands for advective processes. Considering horizontal means in eq. (5), spatial derivatives are evaluated using discrete differentiation scheme, S is calculated as the loss of CO due to its reaction with OH, and Σ is estimated as a residual term, then all budget components are averaged over the half-month periods MA2, AP1 and AP2 as described in Section 6. In the following, we limit the calculations over West Africa within the domain defined in Fig. 3c.

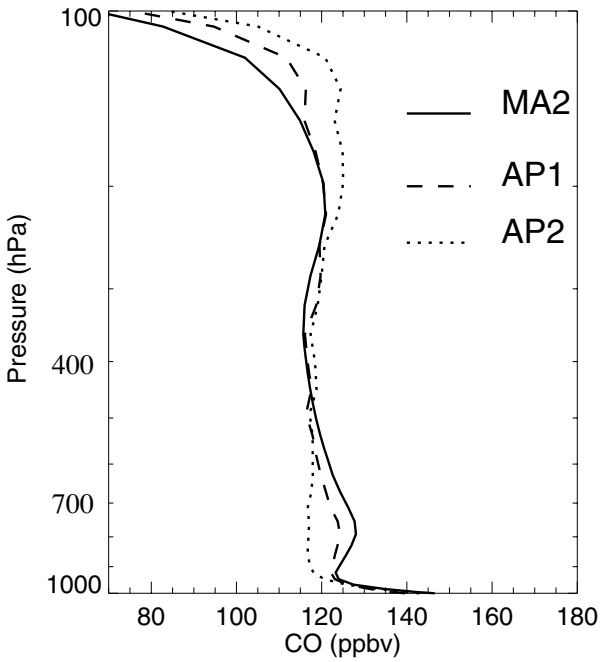

Fig. 8. Mean CO profiles averaged over the domain defined in Fig. 3c and simulated by MOCAGE with assimilation of MOPITT CO for three periods: MA2, AP1 and AP2 (see text).

The profiles of the semi-monthly horizontal mean CO during MA2, AP1 and AP2 indicate concentrations ranging from 110 to 130 ppbv throughout the troposphere tending to increase with time above 500 hPa (Fig. 8). Surface CO mainly caused by biomass burning contributes to the highest CO values (∼150 ppbv) in this region (Gregory et al., 1996), which dramatically decrease down to 120 ppbv at 900 hPa. Then the vertical structure presents small variations up to 150 hPa, with a relative minimum between 300 and 500 hPa. The semi-monthly mean (large-scale) wind components and horizontal wind convergence in Fig. 9 also reveal variations from MA2 to AP2. In particular the mean CO evolution appears to be closely related to a well-marked positive evolution of the vertical velocity (Fig. 9a), suggesting the possible role of the large-scale vertical motions to redistribute CO throughout the troposphere. During AP1 and AP2, the mean vertical motions are mainly upwards, with two layers of

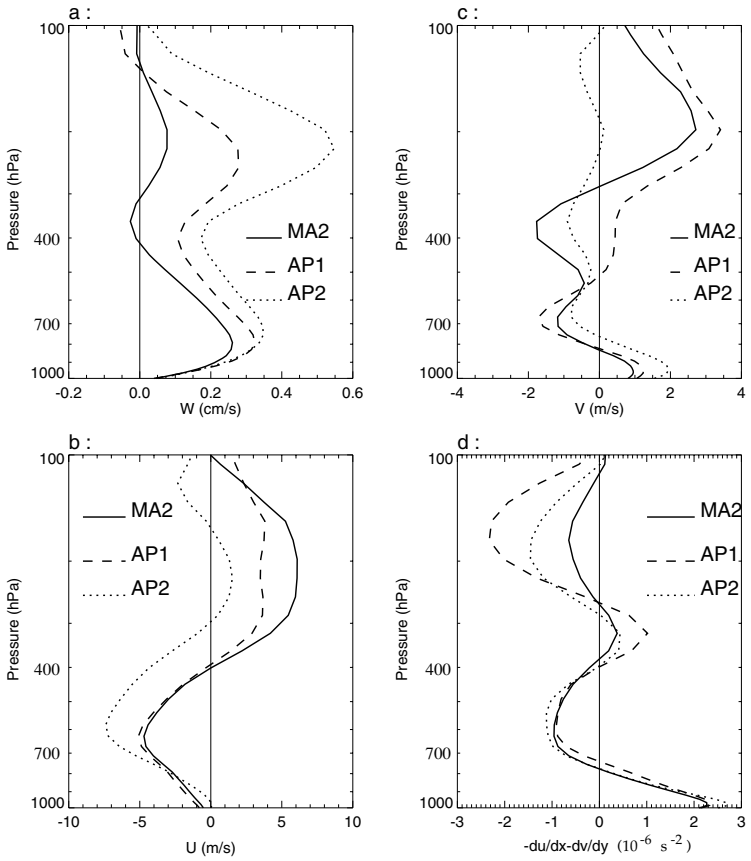

Fig. 9. As in Fig. 8, but for (a) vertical velocity, (b) west-east wind component, (c) south-north wind component and (d) horizontal wind convergence.

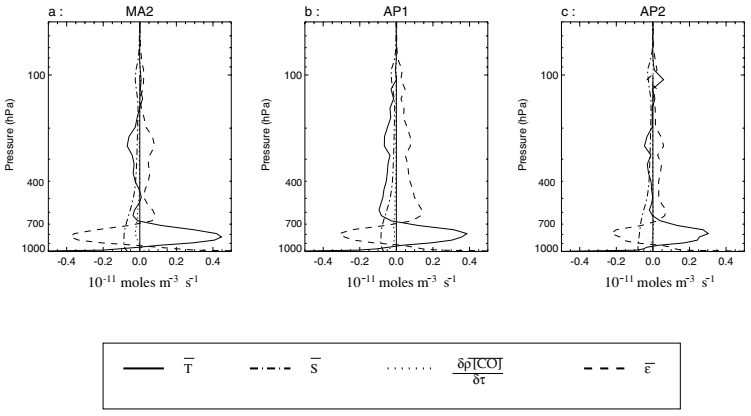

Fig. 10. Mean budget of CO (10^{-11} moles m^{-3} s^{-1}) over Fig. 3 domain simulated by MOCAGE with assimilation of MOPITT CO for the three periods (a) MA2, (b) AP1 and (c) AP2. The solid, dashed, and dashed-dotted lines correspond to total flux convergence, CO source/sink due to subgrid-scale processes and chemical reactions, respectively, the three components of CO Eulerian derivative (dotted line).

pronounced maximum about 800 and 200 hPa, below and above a relative positive minimum at 400 hPa. This differs from the MA2 profile, which exhibits a negative minimum at this level. The average zonal winds (Fig. 9b) also show a clear evolution. For MA2 and AP1, they are easterly in the lower (>400 hPa) troposphere while they turn to westerly above. The easterlies intensify during AP2 while the westerlies (related to the SWJ) progressively decrease due to the onset of the AEJ and TEJ over the region, the effect of which is an apparent negative shift of the zonal wind profile above 650 hPa. Meanwhile the meridional component (Fig. 9c) exhibits a more variable structure with height and time, alternating southerly and northerly flow from the surface to 100 hPa. The horizontal wind variations are associated with the northward displacement of the ITCZ. The mean flow convergence (Fig. 9d) exhibits two marked layers of convergence (minimum below 750–800 hPa and between 400 and 250 hPa) associated with the low- and upper-level vertical velocity maximum (Fig. 9a).

Figure 10 presents the profiles of the semi-monthly CO mean time evolution along with its sources/sinks due to total transport,

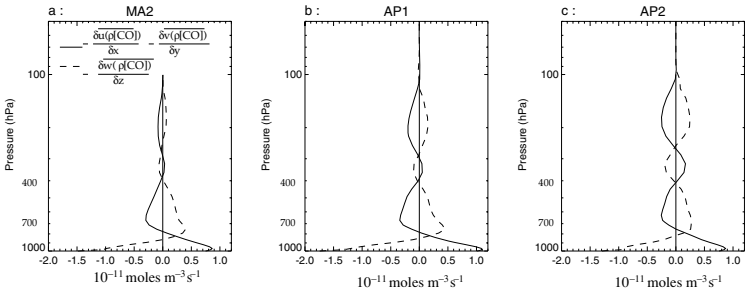

Fig. 11. Mean CO flux convergence profiles (10^{-11} moles m^{-3} s^{-1}) for the three periods MA2 (a), AP1 (b) and AP2 (c). Solid and dashed lines represent horizontal and vertical parts, respectively.

small-scale processes and chemical reactions, according eq. (5). Consistently with Fig. 8, the CO mean tendency during MA2, AP1 and AP2 is negative below 500 hPa. However it is more than an order of magnitude smaller than the different terms that contribute to the CO budget: T, S and Σ. Hence, at each level, the different CO production/loss terms balance each other quite well. Strongest contributions are in the lower (>600 hPa) troposphere: maximum sources and sinks occur between the surface and 800 hPa. At the lowest levels (>950 hPa), sources originate from surface emission and turbulent diffusion whereas advection and OH reaction act as a sink. At levels near 800 hPa, source and sink origins change: large-scale advection supplies this layer with CO while subgrid vertical transport (deep convection) processes generate an upward transport (the 900–700 hPa layer feeds the 700–80 hPa one with CO), while the destruction with OH represents one third to half of the sink.

The partition of the horizontal and vertical flux convergences reveals the respective role of both horizontal and vertical mean transports. Figures 11a–c show that horizontal and vertical mean flux convergences are opposing in most respects. Globally the vertical CO flux convergence (divergence) balances the horizontal flux divergence (convergence), except in the layer ∼850–750 hPa where both horizontal and vertical fluxes act to increase the CO concentration compensating for the sink created by small-scale processes such as convection (Fig. 10). Vertical transports associated with the low-level updraft layer (see Fig. 9a) remove CO present below ∼850 hPa and redistribute it in the upper 850–400 hPa layer. In addition to convection contribution (Fig. 10), this CO uplift helps in maintaining sufficient concentration to balance the loss of CO due to horizontal exports and chemical reactions occurring at these upper levels. Figures 11 and 9(d) strongly suggest that the horizontal CO flux convergence primarily results from the horizontal wind convergence.

Table 1 gives a quantitative synthesis of the relative importance of the budget components in three characteristic layers that can be defined from the above discussion. To evaluate the respective roles of horizontal and vertical resolved transports, subgrid-scale processes and chemical reactions, various terms of eq. (5) (i.e. horizontal convergence, chemical sink, subgrid production/loss and time CO evolution terms) are integrated downwards throughout the depth of each layer and over a unit surface, yielding net changes expressed in moles s^{-1}. The net surface emission (emission + deposition) is deduced from the balance of the budget equation within the total column. The first layer is between 1000 and 800 hPa where the upward motions are important for CO transport to the 800–400 hPa layer (second layer). Finally the rest of the troposphere defines the third layer where smaller contributions are found. The vertical velocity is very small at the top of this layer near 80 hPa, and is assumed to be 0 in order to close the budget. Table 1 indicates that during the three periods MA2, AP1 and AP2, lateral inward transports of CO constitute the major source in the surface layer (52–55% of the total source in each 1000–100 hPa column), indicative that for this season CO emissions outside our reference box are of importance in the local budget. Another lesser source from surface emission of CO (18–31%) is necessary to compensate the loss of CO due to OH reaction (5–6%) and upward top transfer (67–80%). This upward transport from low-level CO fully provides the source of the middle layer (800–400 hPa) since both horizontal exports and chemical processes account for the CO sink (34–46% and 13–16%, respectively) in addition to the loss from upward transport through the top of the considered layer. Finally, the proportion of CO source in the upper layer (<400 hPa) mainly originates from subgrid transport processes (13–22%) and large-scale vertical transports (increasing from 2% to 26%), to balance the horizontal exports and chemical sink.

8. Conclusions

In this paper, we have used CO to analyse transport of pollutants emitted by biomass burning over West Africa during Spring 2001. The study is based on the assimilation of MOPITT CO measurements in the global 3-D chemistry and transport model MOCAGE using a Kalman filter technique. A validation of simulated CO distributions has been performed using MOPITT measurements, CMDL and TRACE-P data. It is found that assimilation has a positive impact on model results, in particular it reduces the strong overestimation over tropical regions, providing more realistic CO fields than the model 'free' simulation. The 4-D assimilated fields obtained, combining realistic information on the dynamics (ARPEGE meteorological analyses) and on the tracer distribution, are well suited to compute CO budgets. Analysis of CO distribution and transport over West Africa during 2001 March and April shows that dry convection resulting

Table 1. Budget of CO over West Africa during MA2, AP1, and AP2. Contributions of transport, unresolved and chemical processes, and CO time evolution (10^{-8} moles s^{-1}) in a unit base column are given for the three layers: surface to 800 hPa, between 800 and 400 hPa, and from 400 to 80 hPa. The percentages indicated in brackets are computed relative to the total influx integrated over the depth of the column (last line)

Process	Surface to 800 hPa		
	MA2	AP1	AP2
CO influx due to biomass burning	0.46 (23%)	0.43 (18%)	0.59 (31%)
Chemical source/sink flux	−0.12 (−6%)	−0.12 (−5%)	−0.12 (−6%)
Influx/outflux due to horizontal transport	1.03 (53%)	1.23 (52%)	1.05 (55%)
CO time evolution flux (× −1)	−0.01 (0%)	0.04 (2%)	0.01 (0%)
Vertical outflux towards the layer above	−1.36 (−70%)	−1.58 (−67%)	−1.53 (−80%)
		800 to 400 hPa	
CO influx from the layer below	1.36 (70%)	1.58 (67%)	1.53 (80%)
Chemical source/sink flux	−0.31 (−16%)	−0.30 (−13%)	−0.28 (−15%)
Subgrid processes	−0.18 (−9%)	0.08 (3%)	−0.09 (−5%)
Influx/outflux due to horizontal transport	−0.89 (−46%)	−1.10 (−46%)	−0.65 (−34%)
CO time evolution flux (× −1)	0.07 (3%)	0.05 (2%)	−0.01 (0%)
Vertical influx from/outflux towards the layer above	−0.05 (−2%)	−0.31 (−13%)	−0.50 (−26%)
		≤400 hPa	
CO outflux towards/influx from the layer below	0.05 (2%)	0.31 (13%)	0.50 (26%)
Chemical source/sink flux	−0.17 (−8%)	−0.17 (−7%)	−0.18 (−9%)
Subgrid processes	0.38 (19%)	0.52 (22%)	0.25 (13%)
Influx/outflux due to horizontal transport	−0.27 (−13%)	−0.67 (−28%)	−0.58 (−30%)
CO time evolution flux (× −1)	0.01 (0%)	0.01 (0%)	0.01 (0%)
Total source	1.95	2.36	1.91

from the confluence between monsoon and Harmattan winds is responsible for the CO upward motion as high as 500 hPa. At this level, a part of the CO is transported westwards by the AEJ, and another part is taken in the secondary circulation of TEJ and SWJ, with CO reaching more easily 200 hPa and also for a fraction to be transported eastwards and westwards within SWJ and TEJ, respectively. Quantitative study of CO budget reveals a balance between total resolved-scale and subgrid-scale transport, as well as chemical contribution, which are the main source/sink of CO. So, when considering the West African troposphere, the main source of CO comes from low levels (surface to 800 hPa) and is associated with biomass burning (∼18–31%) and inflow (∼52–55%). This quantity is then reallocated throughout free troposphere by net horizontal and vertical transports, and evolves via chemical reactions. More than 70% of the CO present in low levels (surface to 800 hPa) is evacuated by transport into the free troposphere. Above 800 hPa, the portion that contributes to the increase in the CO burden represents only a few percents, with outflows and chemical reactions representing important losses. So, most of the CO emitted over West Africa during spring is quickly expelled towards the Atlantic Ocean within the AEJ in the middle troposphere and, both westwards and eastwards in the upper troposphere via SWJ and TEJ, respectively. At present, it is well known that African biomass burning affects Asian and South American chemical budget, and conversely Africa is subject to pollutants coming from neighbouring regions and even from other continents, as suggested by the qualitative importance of the CO inflow. The mechanisms of these global exports and their quantitative impact to the seasonal and annual scales are now being considered with the CTM/assimilation system presented here.

9. Acknowledgments

This work was supported by the French Space Agency, CNES as well as the French National Program on Atmospheric Chemistry (PNCA).

References

Allen, D. J., Kasibhatla, P., Thompson, A. M., Rood, R. B., Doddridge, B. G. and co-authors 1996. Transport induced interannual variability of carbon monoxide determined using a chemistry and transport model. *J. Geophys. Res.* **101**, 28 655–28 670.

Bechtold, P., Bazile, E., Guichard, F., Mascart, P. and Richard, E. 2001. A mass flux convection scheme for regional and global models. *Quart. J. Roy. Meteor. Soc.* **127**, 869–886.

Bey, I., Jacob, D. J., Logan, J. A. and Yantosca, R. M. 2001a. Asian chemical outflow to the Pacific in spring: origins, pathways, and budgets. *J. Geophys. Res.* **106**, 23 097–23 113.

Bey, I., Jacob, D. J., Yantosca, R. M., Logan, J. A., Field, B. D. and co-authors 2001b. Global modeling of tropospheric chemistry with assimilated meteorology: Model description and evaluation. *J. Geophys. Res.* **106**(D19), 23 073–23 095.

Brasseur, G. P., Orlando, J. J. and Tyndall, G. S. 1999. *Atmospheric Chemistry and Global Change*. Oxford University Press, Oxford, 688p.

Cathala, M.-L., Pailleux, J. and Peuch, V.-H. 2003. Improving global chemical simulations of the upper troposphere-lower stratosphere with sequential assimilation of MOZAIC data. *Tellus* **55B**, 1–10.

Cautenet, S., Poulet, D., Delon, C., Delmas, R., Grégoire, J.-M., and co-authors 1999. Simulation of carbon monoxide redistribution over central Africa during biomass burning events (Experiment for Regional Sources and Sinks of Oxidants (EXPRESSO)). *J. Geophys. Res.* **104**, 30 641–30 657.

Cicerone, R. J. 1998. How has the atmospheric concentration of CO changed. In: *The Changing Atmosphere* (eds. F. S. Rowland and I. S. A. Isaken). John Wiley & Sons, New York, 49–61.

Courtier, P., Freydier, C., Geleyn, J.-F., Rabier, F. and Rochas, M. 1991. The ARPEGE project at Météo-France. In: *Workshop on numerical methods in atmospheric models*, **Vol. 2**. ECMWF, Reading, UK, 193–231.

Daniel, J. S. and Solomon, S. 1998. On the climate forcing of carbon monoxide. *J. Geophys. Res.* **103**, 13 249–13 260.

Deeter, M. N., Emmons, L. K., Francis, G. L., Edwards, D. P., Gille, J. C. and co-authors 2003. Operational carbon monoxide retrieval algorithm and selected results for the MOPITT instrument. *J. Geophys. Res.* **108**(D14), 4399, doi:10.1029/2002JD003186.

Deeter, M. N., Emmons, L. K., Edwards, D. P. and Gille, J. C. 2004. Vertical resolution and information content of CO profiles retrieved by MOPITT. *Geophys. Res. Lett.* **31**, L15112, doi:10.1029/2004GL020235.

Dentener, F., Stevenson, D., Cofala, J., Mechler, R., Amann, M., and co-authors 2005. The impact of air pollutant and methane emission controls on tropospheric ozone and radiative forcing: CTM calculations for the period 1990–2030. *Atmos. Chem. Phys.* **5**, 1731–1755, SREF-ID:1680-7324/ap/2005-5-1731.

Drummond, J. R. 1992. Measurements of Pollution in the Troposphere (MOPITT). In: *The Use of EOS for Studies of Atmospheric Physics* (eds. Gille, J. C. and Visconti, G.). North-Holland, Amsterdam, 77–101.

Drummond, J. R. and Mand, G. S. 1996. The Measurements of pollution in the troposphere (MOPITT) instrument: overall performance and calibration requirements. *J. Atmos. Oceanic Technol.* **13**, 314–320.

Dufour, A., Amodei, M., Ancellet, G. and Peuch, V.-H. 2005. Observed and modeled "chemical weather" during ESCOMPTE. *Atmos Res.* **74**, 161–189.

Duncan, B. N. and Bey, I. 2004. A modelling study of the export pathways of pollution from Europe: seasonal and interannual variations (1987–1997). *J. Geophys. Res.* **109**, D08301, doi: 1029/2003JD004079.

Edwards, D. P., Lamarque, J.-F., Attié, J.-L., Emmons, L. K., Richter, A. and co-authors 2003. Tropospheric ozone over the tropical Atlantic: A satellite perspective. *J. Geophys. Res.* **108**(D8), 4237, doi:10.1029/2002JD002927.

Emmons, L. K., Deeter, M. N., Gille, J. C., Edwards, D. P., Attié, J.-L. and co-authors 2004. Validation of Measurements of Pollution in the Troposphere (MOPITT) CO retrievals with aircraft in situ profiles. *J. Geophys. Res.* **109**(D3), D03309, 10.1029/2003JD004101.

Fehsenfeld, F. C., Daum, P., Leaitch, W. R., Trainer, M., Parrish, D. D. and co-authors 1996. Transport and processing of O3 and O3 precursors over the North Atlantic: An overview of the 1993 North Atlantic Regional Experiment (NARE) summer intensive. *J. Geophys. Res.* **101**, 28 877–28 891.

Giglio, L., Kendall, J. D. and Mack, R. 2003. A multi-year active fire dataset for the tropics derived from the TRMM VIRS. *Int. J. Remote Sensing* **24**(22), 4504–4525.

Granier, C., Petron, G., Muller, J.-F. and Brasseur, G. 2000. The impact of natural and anthropogenic hydrocarbons on the tropospheric budget of carbon monoxide. *Atmos. Environ.* **34**, 5255–5270.

Gregory, G. L. et al. 1996. Chemical characteristics of tropospheric air over the tropical South Atlantic Ocean: relationship to trajectory history. *J. Geophys. Res.* **101**, 23 957–23 972.

Hoell, J. M., Davis, D. D., Liu, S. C., Newell, R. E., Akimoto, H. and co-authors 1997. The Pacific Exploratory Mission-West Phase B: February-March. *J. Geophys. Res.* **102**(D23), 28 223–28 240.

Horowitz, L. W., Walters, S., Mauzerall, D. L., Emmons, L. K., Rash, P. J. and co-authors 2003. A global simulation of tropospheric ozone and related tracers: Description and evaluation of MOZART, version 2. *J. Geophys. Res.* **108**(D24), 4784, doi:10.1029/2002JD002853.

Jacob, D. J. and Prather, M. J. 1990. Radon-222 as a test of convective transport in a general circulation model. *Tellus* **42B**, 118–134.

Jacob, D. J., Prather, M. J., Rasch, P. J., Shia, R.-L., Balkanski, Y. J. et al. 1997. Evaluation and intercomparison of global atmospheric transport models using 222 Rn and other short-lived tracers. *J. Geophys. Res.* **102**, 5953–5970.

Jacob, D. J., Crawford, J. H., Kleb, M. M., Connors, V. S., Bendura, R. J. and co-authors 2003. The Transport and Chemical Evolution over the Pacific (TRACE-P) aircraft mission: design, execution, and first results. *J. Geophys. Res.* **108**, 9000, 10.1029/2002JD003276.

Josse, B., Simon, P. and Peuch, V.-H. 2004. Radon global simulations with the multiscale chemistry and transport model MOCAGE. *Tellus* **56B**, 339–356.

Khattatov, B. V., Lamarque, J.-F., Lyjak, L. V., Menard, R., Levelt, P. and co-authors 2000. Assimilation of satellite observations of long-lived chemical species in global chemistry transport models. *J. Geophys. Res.* **105**, 29 135–29 144.

Lamarque, J.-F., Khattatov, B. V. and Gille, J. C. 1999. Assimilation of Measurement of Air Pollution From Space (MAPS) CO in a global three-dimensional model. *J. Geophys. Res.* **104**, 26 209–26 218.

Lefèvre, F., Brasseur, G. P., Folkins, I., Smith, A. K. and Simon, P. 1994. Chemistry of the 1991–1992 stratospheric winter: three-dimensional model simulations. *J. Geophys. Res.* **99**, 8183–8195.

Leroux, M. 2001. The meteorology and climate of Tropical Africa. *Springer-Praxis Books in Environmental Sciences*. Springer-Praxis, Chichester, UK, 548 p.

Liang, Q., Jaeglé, L., Jaffe, D. A., Weiss-Penzias, P., Heckman, A. and co-authors 2004. Long-range transport of Asian pollution to the Northeast Pacific: seasonal variations and transport pathways of carbon monoxide. *J. Geophys. Res.* **109**, D23S07, 10.1029/2003JD004402.

Louis, J.-F. 1979. A parametric model of vertical eddy-fluxes in the atmosphere. *Bound. Lay. Meteor.* **17**, 187–202.

Lorenc, A. C. 1986. Analysis methods for numerical weather prediction. *Quart. J. Roy. Meteor. Soc.* **112**, 1177–1194.

Mari, C., Yano, J.-I., Donner, L. J., Lawrence, M. G., Stohl, A. and co-authors 2003. On moist convection, mesoscale processes and convective transport of gases and aerosols. Workshop report: convective chemical transport. News & Information Service of the EGS. *The Eggs* Issue #5, 21–24, http://www.the-eggs.org/print_articles.php.

Ménard, R., Cohn, S. E., Chang, L.-P. and Lyster, P. M. 2000. Assimilation of stratospheric chemical tracer observations using a Kalman filter. Part I: formulation. *Mon. Wea. Rev.* **128**, 2654–2671.

Michou, M. and Peuch, V.-H. 2002. Echanges en surface dans le modèle chimie-transport multi-échelles MOCAGE. *Rev. Sci. Eau* **15**, 173–204.

Michou, M., Laville, P., Serça, D., Fotiadi, A., Bouchou, P. and co-authors 2005. Measured and modeled dry deposition velocities over the ESCOMPTE area. *Atmos. Res.***74**(1–4), 89–116.

Nho-Kim, E.-Y., Michou, M. and Peuch, V.-H. 2004. Parameterization of size dependent particle dry deposition velocities for global modeling. *Atmos. Env.* **38**(13), 1933–1942.

Nielsen, T. T. 1999. Characterization of fire regimes in the Experiment for Regional Sources and Sinks of Oxidants (EXPRESSO) study area. *J. Geophys. Res.* **104**, 30 713–30 723.

Novelli, P. C., Steele, L. P. and Tans, P. 1992. Mixing ratios of carbon monoxide in the troposphere. *J. Geophys. Res.* **97**(D18), 20 731–20 750.

Novelli, P. C., Masarie, K. A. and Lang, P. M. 1998. Distributions and recent changes of carbon monoxide in the lower troposphere. *J. Geophys. Res.* **103**(D5), 19 015–19 033.

Olivier, J. G. J., Bouwman, A. F., Van der Maas, C. W. M., Berdowski, J. J. M., Veldt, C. and co-authors 1996. Description of EDGAR Version 2.0: a set of global emission inventories of greenhouse gases and ozone-depleting substances for all anthropogenic and most natural sources on a per country and on $1^\circ \times 1^\circ$ grid. *RIVM Rep 77060002/TNO MEP report nr. R96/119* RIVM, Bilthoven, The Netherlands.

Pan, L., Gille, J. C., Edwards, D. P., Bailey, P. L. and Rodgers, C. D. 1998. Retrieval of tropospheric carbon monoxide for the MOPITT experiment. *J. Geophys. Res.* **103**, 32 277–32 290.

Peuch, V.-H., Amodei, M., Barthet, M., Cathala, M.-L., Josse, B. and co-authors 1999. MOCAGE: Modèle de Chimie Atmosphérique à Grande Echelle. *Actes des Ateliers de Modélisation de l'Atmosphère*. Météo-France, Centre National de Recherches Météorologiques, 33–36.

Rodgers, C. D. 1990. Characterization and error analysis of profiles retrieved from remote sounding measurements. *J. Geophys. Res.* **95**, 5587–5595.

Rodgers, C. D. 2000. Inverse methods for atmospheric sounding: Theory and practice. *Series on Atmospheric, Oceanic and Planetary Physics*, **Vol. 2**. World Scientific, Singapore, New Jersey, London, Hong Kong, p. 238.

Spivakovsky, C. M., Logan, J. A., Montzka, S. A., Balkanski, Y. J., Foreman-Fowler, M. and co-authors 2000. Three-dimensional climatological distribution of tropospheric OH: Update and evaluation. *J. Geophys. Res.* **105**(D7), 8931–8980.

Stockwell, W. R., Kirchner, F., Khun, M. and Seefeld, S. 1997. A new mechanism for regional atmospheric chemistry modelling. *J. Geophys. Res.* **102**, 25 847–25 879.

Stohl, A., Eckhardt, S., Forster, C., James, P. and Spichtinger, N. 2002. On the pathways and timescales of intercontinental air pollution transport. *J. Geophys. Res.* **107**, 4684, doi: 10.1029/2001JD001396.

Thompson, A. M. 1992. The oxidizing capacity of the earth's atmosphere: Probable past and future changes. *Science* **256**, 1157–1165.

Yanai, M., Esbensen, S. and Chu, J. H. 1973. Determination of bulk properties of tropical cloud clusters from large-scale heat and moisture budgets. *J. Atmos. Sci.* **30**, 611–627.